

In vivo ultrahigh-resolution optical coherence tomography of mouse colon with an achromatized endoscope

Alexandre R. Tumlinson

University of Arizona
Division of Biomedical Engineering
Tucson, Arizona 85721
and
Medical University of Vienna
Center of Biomedical Engineering and Physics
Christian Doppler Laboratory
Vienna, Austria

Boris Považay

Medical University of Vienna
Center of Biomedical Engineering and Physics
Christian Doppler Laboratory
Vienna, Austria

Lida P. Hariri

University of Arizona
Division of Biomedical Engineering
Tucson, Arizona 85721

James McNally

University of Arizona
Optical Sciences Center
Tucson, Arizona 85721

Angelika Unterhuber

Boris Hermann

Harald Sattmann

Wolfgang Drexler

Medical University of Vienna
Center of Biomedical Engineering and Physics
Christian Doppler Laboratory
Vienna, Austria

Jennifer K. Barton

University of Arizona
Division of Biomedical Engineering
Tucson, Arizona 85721
and
University of Arizona
Optical Sciences Center
Tucson, Arizona 85721

1 Background and Introduction

1.1 *In Vivo* Monitoring of Colon Disease in Mice

Many mouse models for studying human colon pathology exist and are under continual development (see Table 1). It is interesting to determine the state of disease *in vivo* for serial

Abstract. Endoscopic ultrahigh-resolution optical coherence tomography (OCT) enables collection of minimally invasive cross-sectional images *in vivo*, which may be used to facilitate rapid development of reliable mouse models of colon disease as well as assess chemopreventive and therapeutic agents. The small physical scale of mouse colon makes light penetration less problematic than in other tissues and high resolution acutely necessary. In our 2-mm diameter endoscopic time domain OCT system, isotropic ultrahigh-resolution is supported by a center wavelength of 800 nm and full-width-at-half-maximum bandwidth of 150 nm (mode-locked titanium:sapphire laser) combined with 1:1 conjugate imaging of a small core fiber. A pair of KZFSN5/SFPL53 doublets provides excellent color correction to support wide bandwidth throughout the imaging depth. A slight deviation from normal beam exit angle suppresses collection of the strong back reflection at the exit window surface. Our system achieves axial resolution of 3.2 μm in air and 4.4- μm lateral spot diameter with 101-dB sensitivity. Microscopic features too small to see in mouse tissue with conventional resolution systems, including colonic crypts, are clearly resolved. Resolution near the cellular level is potentially capable of identifying abnormal crypt formation and dysplastic cellular organization. © 2006 Society of Photo-Optical Instrumentation Engineers. [DOI: 10.1117/1.2399454]

Keywords: ultrahigh resolution optical coherence tomography (UHR-OCT); endoscope; catheter; mouse; gastrointestinal (GI); colon; achromatic.

Paper 06092RR received Apr. 6, 2006; revised manuscript received Aug. 21, 2006; accepted for publication Aug. 21, 2006; published online Nov. 28, 2006. This paper is a revision of a paper presented at the SPIE conference on Advanced Biomedical and Clinical Diagnostic Systems, Jan. 2005, San Jose, Calif. The paper presented there appears (unrefereed) in SPIE Proceedings Vol. 5692.

studies in which the progress of disease is monitored and to determine, prior to sacrifice, if disease has occurred. Minimally invasive methods promise to reduce the cost and time to develop new breeds of disease model mice and to evaluate chemopreventive and therapeutic agents. A slightly modified pediatric cystoscope (2.1-mm diameter) has been used by other groups to visualize the luminal surface of the murine

Address all correspondence to Alexandre R. Tumlinson, 1230 E. Speedway Blvd., Tucson, AZ 85721-0104; Tel: 520-626-8175; Fax: 520-621-8076; E-mail: atumlins@email.arizona.edu

Table 1 Mouse models of cancer large intestine/colon/rectum. Summarized from Boivin et al. (Ref. 17) unless otherwise noted. (AOM, azoxymethane; DMH, dimethylhydrazine; DSS, dextran sodium sulfate; MNG, *N*-methyl-*N'*-nitro-*N*-nitrosoguanidine; PI, phosphoinositide; NR, not reported.)

Name of Model	Predominant Neoplasm	Metastasis
MMR genes		
APC ^{min/+}	Adenoma	No
APC ^{min/+} w/arginine ^a	Adenoma	No
APC ^{1638/+}	Adenoma/carcinoma	No
TGF-β models		
Rag2 ^{-/-} Tgfβ1 ^{-/-}	Mucinous carcinoma	No
Rag2 ^{-/-} Tgfβ1 ^{+/-}	Adenoma	No
Smad3 ^{-/-}	Mucinous carcinoma	Yes
Immunodeficient		
Interleukin-10 ^{-/-}	Colitis/carcinoma	No
Interleukin-2	Carcinoma	No
Tcrα ^{-/-}	Colitis	
Gα _{i2} ^{-/-}	Colitis/carcinoma	No
Carcinogen-treated		
AOM (DMH)	Adenoma/carcinoma	NR
AOM w/DSS ^b	Adenoma/carcinoma	
MNG	Adenoma/carcinoma	NR
Other models		
Cdx2 ^{+/-}	Gastric and intestinal heteropia	No
Muc2 ^{-/-}	Adenoma/carcinoma	No
PI 3-kinaseγ ^{-/-}	Carcinoma	Peritoneal

^aReference 18.

^bReference 19.

descending colon (distal 3 cm) and shows crypt detail when exogenous dyes are used.^{1,2} Optical coherence tomography (OCT) provides minimally invasive, cross-sectional images that indicate the thickness and scattering density of underlying tissue and is readily adapted to small diameter endoscopic applications. This technology has been shown to differentiate pathology from normal states in the human gastrointestinal (GI) tract.³ The minute scale of the mouse presents a challenge, not only in packaging but also in resolution. Standard resolution OCT endoscopy in the mouse has clearly shown the layered structure of the colon wall and gross tissue abnormalities but has failed to resolve smaller features such as the colonic crypts where adenoma are believed to develop.^{4,5} We aim to create an endoscopic ultrahigh-resolution OCT (UHR-

OCT) system capable of resolving colonic crypt structure in the mouse.

1.2 Optical Considerations in Ultrahigh-Resolution OCT Endoscopes

To date, the majority of side-firing OCT endoscopes have utilized a similar optical design consisting of a single-mode fiber glued directly to a gradient index (GRIN) lens, which is in turn cemented to a prism that redirects the light out the side of a transparent window. The light then comes to a focus at a set distance outside the endoscope window. Advantages of this design are low cost, ease of manufacture, and mechanical stability due to its monolithic, alignment free construction. Herz et al. have pushed the limits of axial resolution in the conventional GRIN lens-based endoscope design to 5 μm in air by extending the bandwidth of the source (centered at 1300 nm) and carefully matching the dispersion in the reference arm. These improvements have allowed improved visualization of rabbit GI tissues including the crypts in the colon.⁶ Unfortunately, the lateral point spread function (PSF) of this (and other) traditional GRIN lens-based endoscopes is relatively poor, with spot diameters on the order of 15 μm. The imaging conjugates are greater than 1:1 because one end of the fiber is in contact with the GRIN lens and a positive working distance is required to focus at some depth within the tissue; therefore the lateral resolution is larger than the mode field diameter of the fiber.

Utilizing a shorter central wavelength simultaneously improves the theoretical axial resolution for a given bandwidth and improves the lateral resolution for a given numerical aperture. However, the linear and nonlinear dispersion of materials including silica fibers and GRIN lenses increases substantially as wavelengths are shortened from 1300 nm toward 800 nm. Additional nonlinear dispersion suggests that greater care should be taken when matching dispersion in the sample and reference arms, while greater linear dispersion dictates improved management of axial chromatic error in the objective lens. The intensity of the light collected by an OCT system is strongly dependent on how near (in the axial direction) the scattering surface is to the beam focus. Uncorrected axial chromatic aberration causes each wavelength to be focused at a different depth. Usually, shorter wavelengths are focused at a shorter distance than longer wavelengths. If a scattering surface lies closer to the focal plane of one color than another, the intensity of the reflected spectrum is skewed toward that color. The resulting effective bandwidth of the light returned from any particular depth will usually be narrower than that of the source, thereby reducing axial resolution.⁷ Although microoptic systems are more forgiving than larger systems, because chromatic aberration scales with the focal length of the lens, chromatic aberration must be considered to advance past the current state of the art in UHR-OCT endoscopy.

A further optical consideration is the suppression of unwanted reflections in the optical system. Back reflections in the sample arm limit the usable detector range and may cause disturbing image artifacts if they lie close to the target tissue. The specular back reflection of the inner surface of the window between the imaging optics and the tissue can be very strong because it lies close to focus. Herz et al. used index matching fluid inside the endoscope to suppress this

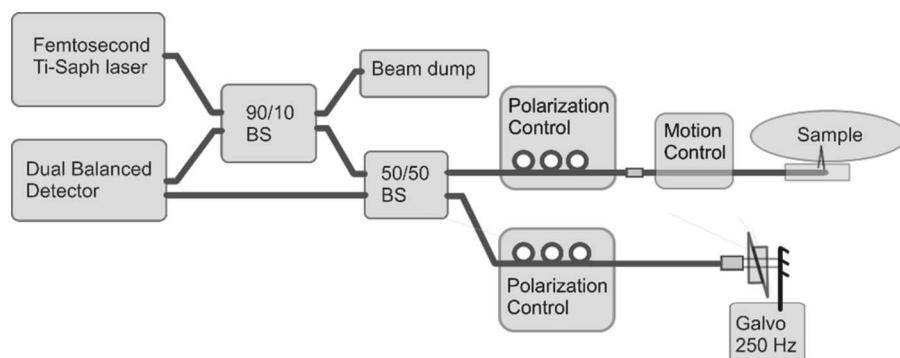


Fig. 1 Optical subsystem diagram. Endoscopic sample arm is butt coupled to a time domain OCT system using a sub-10-fs Ti:sapphire laser source (800-nm center wavelength, 150-nm FWHM bandwidth) and a fiber beamsplitter which directs 10% of the source light into the interferometer and 90% of the return light to the dual balanced detector. The reference arm utilizes a short distance of higher second-order dispersion materials to allow a greater air space than is found in the sample arm.

reflection.⁶ A design by Li et al. used a beam that exited the envelope at an oblique angle for better Doppler flow resolution in an artery.⁸ An off-normal beam exit angle also suppresses the collection of specular back reflection from the window surface.^{9,10}

1.3 Current Work

In the current work, we demonstrate an achromatized UHR-OCT endoscope optimized for use in the mouse colon with 800-nm center wavelength. We compare the theoretical coupling efficiency of this endoscope with a GRIN lens design using commercial ray tracing software. The constructed endoscope was characterized for through-focus bandwidth, axial resolution, signal to noise, and lateral spot diameter. This endoscope maintains a stable wide bandwidth centered around 800 nm, while achieving a small beam waist—a task we believe cannot be achieved by the conventional GRIN design. *In vivo* performance is demonstrated in mouse colon.

2 Materials and Methods

2.1 Endoscopic UHR-OCT Setup

A previously described time domain UHR-OCT engine was employed in the present study.^{7,11} The system consists of a sub-10-fs mode-locked titanium:sapphire INTEGRAL PRO laser source (800-nm center wavelength, up to 150-nm full-width-at-half-maximum (FWHM) optical bandwidth) integrated in a fiber-optic-based Michelson interferometer employing a high speed scanning reference mirror (up to 250 Hz, 400 mm/s), dual balanced detection, and phase resolved data sampling. All components of the fiber-optic interferometer were designed to support the propagation of greater than 250-nm bandwidth light throughout the OCT system and to compensate for polarization and dispersion mismatch between the sample and reference arms of the interferometer (see Fig. 1).

A new endoscopic sample arm was designed and constructed for use with the above system and mouse colon imaging. The working distance was selected to be 200 μm in air, corresponding approximately to half the normal thickness of a mouse colon, at the base of the mucosal layer. An imaged spot diameter of 4.4 μm provides a good balance between high lateral resolution at focus and acceptable defocus

through a 400- μm imaging thickness without a dynamically focusing element. This lateral dimension is approximately the mode field diameter of the single-mode fiber used, so a symmetric 1:1 imaging conjugate system was designed. The focusing optics (Fig. 2), a pair of KZFSN5/SFPL53 doublets (custom manufactured by Bern Optics, Westfield, Massachusetts), provide excellent primary and secondary color correction as well as diffraction limited on-axis imaging (Fig. 3), to maintain wide bandwidth through the imaging depth. Two approaches are used to suppress back reflection in the air-spaced tip optics. First, at the fiber output interface, a 1-mm-thick fused-silica spacer is cemented. The resulting index matching suppresses the initial back reflection at the fiber interface; in a design with an angle polished fiber, the mating silica spacer can be used to minimize beam deflection and allow the design to be built with on-axis alignment in a tube (Fig. 4). Second, a slight deviation from normal beam exit angle avoids collection of the strong back reflection at the uncoated exit window surface. The endoscope operates mechanically like other push-pull longitudinally scanning endoscopes^{4,12} by translating an inner lumen connected to the focusing optics relative to an outer lumen connected to sealed window at the endoscope tip.

Ideally, both arms of the interferometer consist of identical materials so that, for each wavelength, an equal time is required to traverse the sample and reference arms. Our sample arm consists almost entirely of germanium-doped silica single-mode fiber, with small thicknesses of exotic glasses used in the doublets, and a minimal amount of air separation between optical elements. The reference arm consists of a fiber of identical material to the endoscope, an achromatized

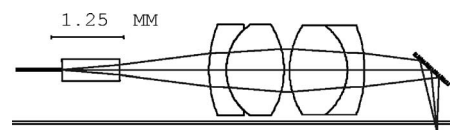


Fig. 2 Optical model of the beam path in the endoscope tip. Two identical KZFSN5/SFPL53 doublets image the source fiber into the tissue at 1:1 conjugates. A 1-mm silica spacer at the fiber output and a 6-deg off-normal beam path at the exit window suppress back reflections.

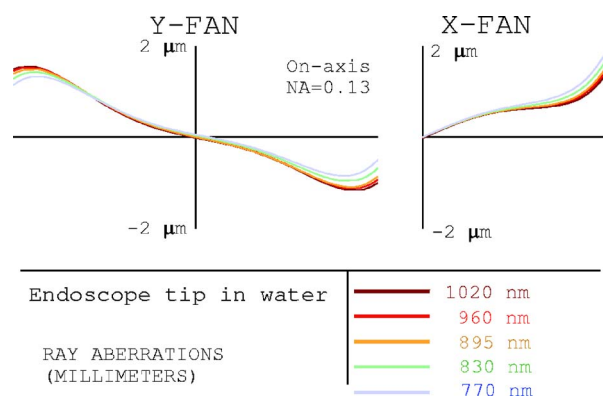


Fig. 3 Ray fan plots show geometrical aberrations much smaller than the diffraction limited spot diameter. Chromatic aberration is very small over the designed range of wavelengths and pupil aberrations are dominated by astigmatism from the cylindrical window immersed in water. The horizontal axis is pupil position, while the vertical axis is transverse ray error at an image plane. The horizontal axis in the sagittal ray fan (left) is plotted from the bottom of the pupil to the top of the pupil, while the tangential ray fan (right) is, because of symmetry, plotted only from the center of the pupil to the extreme right (or left) side. The extrema of the horizontal axis corresponds to the edge of the 0.13 numerical aperture over which the plot was calculated. For more detail, see Ref. 20.

collimator, a section of dispersion compensating glasses, and a translating reference mirror. The fiber length on the reference arm side was made 6 cm shorter than the endoscope and replaced with glass with a higher second-order dispersion (BK7). This glass compensates second-order dispersion while allowing the insertion of a short air gap in the reference arm for the collimator and the translating reference mirror.

2.2 Evaluation of Spectral Transmission by Endoscope Sample Arm through Focus

A key parameter to judge performance of an achromatized sample arm design is the variation in spectral throughput as sample depth changes. Software simulation was performed on the achromatized endoscope as well as a GRIN lens-based endoscope with a proximal glass spacer to yield comparable 1:1 imaging conjugates. Experimental verification of through-focus transmission was performed with the constructed achromatized endoscope.

CODE V lens design software (Optical Research Associates,

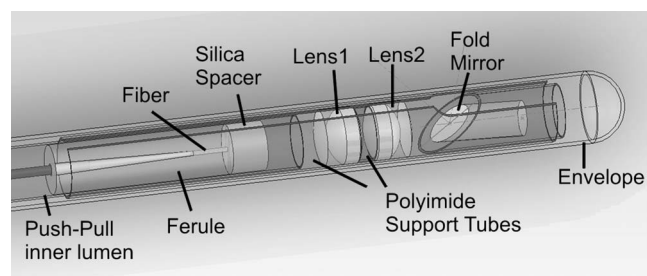


Fig. 4 Solid model shows the mechanical construction of the endoscope tip. The outer dimension of the tubing is 2 mm. The scanning range is 35 mm. All parts are designed to be aligned by location in tight tolerance polyimide tubing.

Pasadena, California) was used to calculate the wavelength-dependent coupling efficiency associated with propagating a Gaussian spatial distribution of light through an optical system, to a mirror located near focus, back through the optical system, and back into a fiber.^{13,14} The distance to the mirror was varied through the imaging depth of the endoscope to predict the change in coupling efficiency in each design. This analysis took into account chromatic and pupil aberrations, as well as diffraction from apertures but did not consider losses due to reflections or transmission of the materials. The coupling efficiency function was then multiplied by a spectrally Gaussian source function to demonstrate how the sample arm optics distort the spectrum as a function of image depth.

A 1:1 imaging conjugate GRIN endoscope was modeled with the following prescription: the source fiber [800-nm center wavelength, 260-nm FWHM bandwidth, 5.4- μm mode field diameter, numerical aperture (NA)=0.13] was in contact with a 2.0-mm BK7 spacer, cemented to a 0.21-pitch GRIN lens (using the CODE V built-in glass definition for SLW 1.0 from NSG America) that was further cemented to a 1.0-mm prism of BK7, and then separated by a 0.4-mm airspace to the 0.1-mm-thick fused-silica cylindrical window with an outer diameter of 2.0 mm, which finally resulted in a focus 0.2-mm deep in a water media. The achromatic doublet design was prescribed with an identical source and fiber, the fused-silica spacer and doublet pair shown in Fig. 3, and an identical window and water media. In both cases, the small deviation from normal incidence at the fused-silica window was omitted from the simulation for simplicity.

The ability of the achromatized endoscope to maintain a 260-nm FWHM bandwidth through focus was verified experimentally. Light from a sub-5-fs Ti: sapphire laser source [800-nm λ_0 , 260-nm $\Delta\lambda$ (FWHM)] was coupled into the endoscope via a fiber beamsplitter and subsequently focused by the endoscope onto a mirror that translated axially through focus. The light was coupled back into the endoscope, through the fiber beamsplitter and subsequently measured by a spectrometer. Through-focus spectra were measured in 50- μm intervals from contact with the endoscope outer window (focus $-200\ \mu\text{m}$) to the far side of focus (focus $+380\ \mu\text{m}$).

2.3 Measurement of PSF

The lateral focused spot dimension predicted by lens design software was tested for a single wavelength ($\sim 830\ \text{nm}$) using a microscope to magnify the focused spot across an inexpensive complementary metal-oxide semiconductor image array. The microscope magnification was calibrated with a test target placed at focus. This microscope also allowed measurement of the working distance to focus. The axial PSF was characterized as the FWHM of the interference fringe envelope resulting from a mirror near focus in air. This result was corrected for a resolution in tissue by dividing by the average index of refraction of 1.4.

2.4 Sensitivity Measurement

Sensitivity was measured with a slight modification to a common method.¹⁵ Typically, power in the sample arm is strongly attenuated by placing a neutral density (ND) filter in the sample arm optics so that a weak, but clearly distinguishable peak can be measured from a mirror placed at focus. The

signal strength is determined by the maximum height of this interferogram (S_{OCT}). The target mirror is removed and the noise is estimated from the variance of the remaining collected data (σ^2). The sensitivity is increased by a factor accounting for the attenuation of the ND filter, yielding an equation for sensitivity (Σ)

$$\Sigma = 10 \log_{10} \left(\frac{S_{OCT}^2}{\sigma_{noise}^2} \right) + 20ND. \quad (1)$$

In the endoscope, however, no neutral density filter can be placed in the beam path due to physical limitations. The efficiency of coupling to the sample arm was therefore reduced by loosening the fiber butt coupling. The magnitude of attenuation was calibrated by measuring the power exiting the sample arm before and after attenuation. The signal was measured with the attenuated arrangement. Because some noise may be introduced by back reflections at the misaligned butt coupler or from reflections in the endoscope, the noise was measured with the fiber efficiently coupled but with no target at the sample plane.

The tomogram's dynamic range was calculated by comparison of the brightest pixels found near focus to the variance of the noise in the region near the top of the tomogram occupied by the clear glass window.

2.5 Measurements in Tissues

Two normal mice were imaged once each with the above-described endoscope. All procedures were approved by the Medical University of Vienna Animal Use Committee. The mice were first anesthetized with a Ketamine-Xylazine mixture (100 mg/kg+10 mg/kg) delivered by intraperitoneal injection, yielding approximately 30 min of working time. The endoscope and anus were thoroughly coated with water-based lubricant before inserting the device to a depth of 33 mm. B-scans of length 30 mm and depth 0.5 mm were collected at a lateral imaging speed of 1.9 mm/s with 900- μ W power incident on the tissue. Shorter, partial length scans were collected with a lateral imaging speed of 0.5 mm/s.

3 Results

3.1 Transmission of Spectra by Endoscope Sample Arm through Focus

Comparison of the simulations of the GRIN-based endoscope and the achromatized endoscope (Fig. 5) illustrates the benefit of using achromatized optics. The transmitted spectrum of the GRIN system shows large changes in spectral shape and peak wavelength through focus. In the current design, using a pair of achromatic doublets, the expected shape of the transmitted spectra is essentially the same as the source and is flatly attenuated away from focus. The lenses are chromatically corrected over a very wide range and good performance is predicted for bandwidths in excess of 400 nm.

The experiment to verify through focus transmission for the achromatized endoscope demonstrated a FWHM bandwidth of 260 nm passed with minimal distortion though the imaging depth of the endoscope (Fig. 6). Some of the distortion that is seen in this experiment, which is not seen in the theoretical curves of Fig. 5, can be attributed to the more

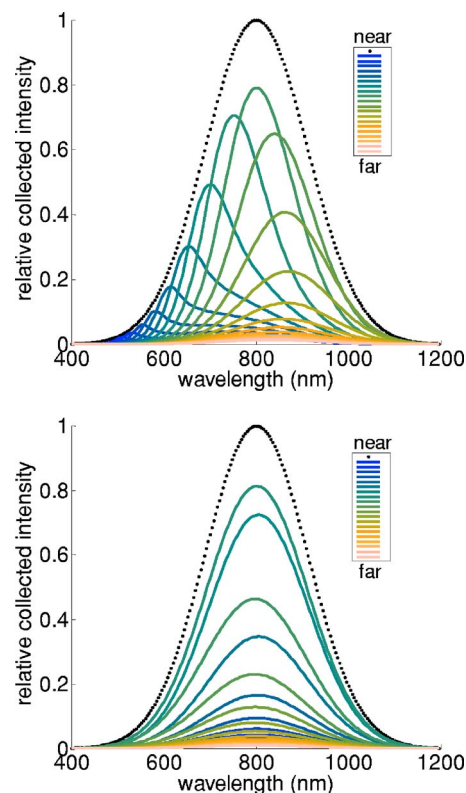


Fig. 5 Comparison of theoretical transmitted spectra by GRIN lens-based endoscope (top) and achromatized endoscope (bottom). The outer dotted line indicates a Gaussian source spectrum with center wavelength at 800-nm and 260-nm FWHM bandwidth. Each solid line represents theoretical transmitted spectra given by multiplying the source spectra by the wavelength-dependent coupling efficiency for a particular placement of a mirror near focus. The axial location of the mirror relative to the focusing optics is encoded in the line shading as indicated by the legend. Lines are separated by 30 μ m of mirror displacement.

Gaussian shape of the idealized source function, which tends to smooth out differences at the tails of the spectrum.

3.2 Axial, Lateral Resolution, and Sensitivity

The lateral spot dimension was measured [Fig. 7(b)] with a calibrated microscope to be 4.4- μ m FWHM at focus. Axial resolution with a 150-nm FWHM bandwidth laser (1.9- μ m theoretical axial resolution in air) was measured [Fig. 7(a)] to be 3.2 μ m in air corresponding to 2.3 μ m in tissue. The broadening of the axial PSF is primarily a result of high-order dispersion resulting from glass type mismatch in the reference arm. Sensitivity of 101 dB was measured at an imaging sample arm power of 900 μ W. Dynamic range found in tissue tomograms (47 dB) is consistent with this estimate of sensitivity.

3.3 In Vivo Imaging

Ultrahigh-resolution tomograms of normal mice (Figs. 8 and 9) show sensitivity to features unresolved by standard resolution systems. Most striking in the comparison between histology of normal mouse colon and our tomograms is that we appear to be able to resolve the boundaries between crypts. These show up as slightly off-vertical lines of hyperintense

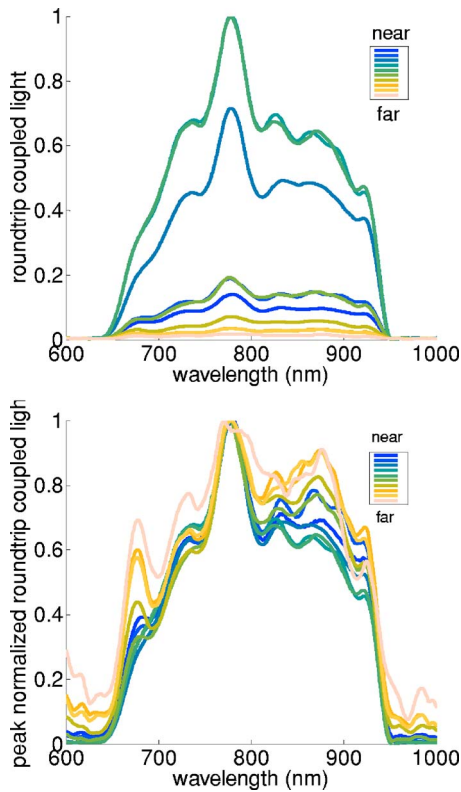


Fig. 6 Experimental data shows that the achromatized endoscope maintains a wide bandwidth through focus. Top frame shows coupled intensity attenuated as mirror moves away from focus. Frame below shows the same data with peak normalization. The axial location of the mirror relative to the focusing optics is encoded in the line shading, as indicated by the legend. Mirror displacement between individual lines is 50 μm .

scatter contained wholly within the mucosa. These real structures contrast to shadowing artifacts observed within the muscular layers that present as perfectly vertical (axially oriented) hypointense stripes that persist beyond tissue boundaries to the bottom of the image. A thin hypointense band about 30- μm -thick caps most of the simple columnar mucosa. This feature is absent in the stratified squamous epithelia of the anal region (Fig. 8). Comparison with histology suggests this may correspond to a single cell layer of absorptive cells lining the luminal surface (Fig. 9). Resolution of the layers of the colon—colonic mucosa, muscular mucosa, submucosa, muscularis externa (inner circular layer and outer longitudinal layer), and serosa—is also clear. We also see lymphoid aggregates either in the mucosa, where they may disrupt the normal distribution of crypt glands or in the submucosa, where they do not disturb the glandular organization but distort the rest of the tissue.

4 Discussion

UHR-OCT images obtained using a 800-nm center wavelength source penetrate the entire thickness of mouse colon tissue and exhibit higher axial and lateral resolution than could be achieved with similar bandwidth and numerical aperture near 1300 nm. We believe these advantages outweigh the disadvantages of higher dispersion in the fiber and optics,

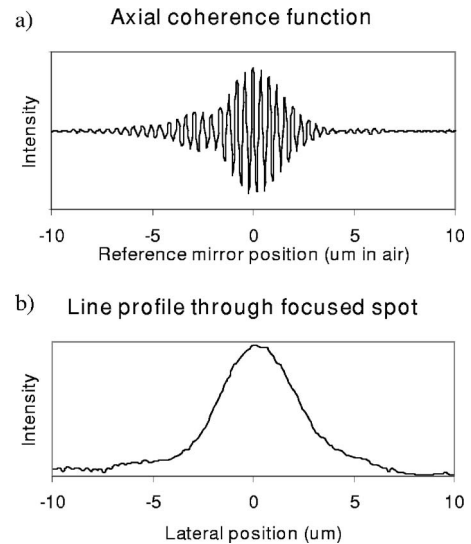


Fig. 7 The axial coherence function (a) indicates an axial resolution of 3.2 μm in air (FWHM). A line profile through an image of the focused spot (b) indicates a 4.4- μm lateral spot diameter (FWHM).

the smaller fiber core diameter that makes efficient fiber coupling more difficult, and the lack of commercial broadband fiber circulators. While we are extremely excited with the improvement in information content in the *in vivo* mouse colon tomograms, there is still room for improvement in axial and lateral information content of our tomograms. For example, Herz et al. demonstrate a direct approach to better match the dispersion by including an air gap in the coupling to the endoscopic sample arm,⁶ which may allow us to achieve the axial resolution potential made possible by achromatized optics and sub-5-fs laser systems at 800-nm center wavelength. The tomograms presented in this work are slightly under-sampled in the lateral direction. Memory limitations of the

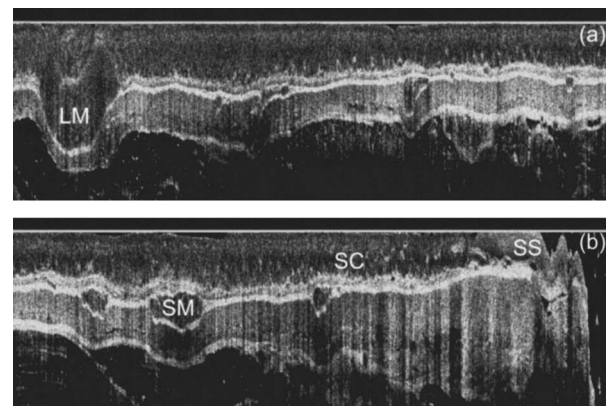


Fig. 8 *In vivo* UHR-OCT tomogram of the distal 30 mm of normal mouse colon (full-length scan, 1.9-mm/s lateral imaging speed). The vertical dimension is 0.4 mm (about 10 \times stretched). A lymphoid aggregate in the mucosa (LM) disturbs the glandular structure, while a lymphoid aggregate in the submucosa (LS) simply inserts itself between the muscular layers; both structures are typical in normal colon. The texture of the mucosa undergoes a visible change as the simple columnar epithelium (SC) gives way to stratified squamous epithelium (SS) in the anal canal.

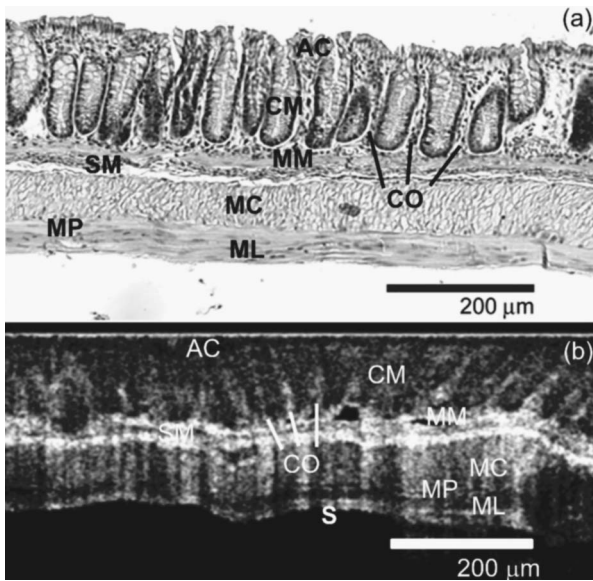


Fig. 9 Detail of *in vivo* UHR-OCT tomogram (partial scan, 0.5-mm/s lateral imaging speed, isotropic scale) of normal mouse colon (b) is compared to an age- and/or strain-matched histology image (a). The colonic mucosa (CM), muscular mucosa (MM), submucosa (SM), circular muscular (MC), longitudinal muscular (ML), and serosa (S) layers are clearly differentiable. The hypointense regions between the outer muscular layers probably correspond to the myenteric plexus (MP) innervating the smooth muscle. Note the nearly vertical structures in the mucosa that may correspond to crypt outlines (CO) and the thin hypointense band near the top of the image that may correspond to a single cell layer of absorptive cells (AC) lining the luminal surface.

data acquisition board allowed acquisition of only 4000 A-scans in a continuous B-scan, resulting in full-length images sampled every $7.5 \mu\text{m}$. Stiction in the tubing used to drive the lateral scan forced a minimum velocity of the probe for smooth translation on shorter scans. The maximum A-scan rate of the time domain OCT system resulted in images sampled every $2 \mu\text{m}$. We foresee an improvement in clarity of crypt outlines and general tomogram sensitivity with a small degree of lateral oversampling. Although the speed at which stiction presents a problem to push-pull endoscopes may be reduced by mechanical design, the final solution may lie in the faster A-line rates achievable with frequency domain OCT systems.¹⁰

The achromatized optics demonstrated here result in transmitted spectra that are uniform through focus. In concept, controlling chromatic aberration is a critical component of UHR-OCT that is as essential in endoscopy as it is in bulk optic systems. Uniformly transmitted spectra are also a critical starting point to spectroscopic OCT.¹⁶ Further modeling and experimental verification is required to establish the allowable chromatic error for a particular source bandwidth and imaging goal.

The tomograms presented here clearly resolve cross-sectional colonic crypt formation in the living mouse without application of exogenous dyes.² We are confident that the present resolution improvements will allow us to better observe disease progression *in vivo* in the smallest common mammalian colon disease model animal. Next-generation ex-

periments focusing on diseased mice will help establish diagnostic criteria in OCT images and determine how criteria proposed in humans and other models can be applied to mice. The reward for careful optical design will be obtained when endoscopic UHR-OCT, including diagnostic criteria obtained from well-understood mouse models, is applied to a poorly understood model and knowledge is accumulated at a lower cost than with currently available techniques.

Acknowledgments

Support for this project includes support from the following sources: NIH Small Animal Imaging Resource CA83148, NIH Grant No. CA109835, University of Arizona Imaging Small Grant, 301 Imaging grant, FWF P14218-PSY, FWF Y 159-PAT, CRAF-1999-70549, the Christian Doppler Society, FEMTOLASERS GmbH, and the Fulbright Commission. The authors would also like to thank Renate Pflug, Peter Ahnelt, Heinz Huemer, and Ulrike Libal for their support of the mice and protocol issues and Faith Rice and Elizabeth Kanter for help with histology.

References

1. E. H. Huang, J. J. Carter, R. L. Whelan, Y. H. Liu, J. O. Rosenberg, H. Rotterdam, A. M. Schmidt, D. M. Stern, and K. A. Forde, "Colonoscopy in mice," *Surg. Endosc* **16**, 22–24 (2002).
2. C. Becker, M. C. Fantini, C. Schramm, H. A. Lehr, S. Wirtz, A. Nikolaev, J. Burg, S. Strand, R. Kiesslich, S. Huber, H. Ito, N. Nishimoto, K. Yoshizaki, N. Nishimoto, P. R. Galle, M. Blessing, S. Rose-John, and M. F. Neurath, "TGF-beta suppresses tumor progression in colon cancer by inhibition of IL-6 trans-signaling," *Immunity* **21**, 491–501 (2004).
3. B. Shen and G. J. Zuccaro, "Optical coherence tomography in the gastrointestinal tract," *Gastrointest Endosc Clin. N. Am.* **14**, 555–571 (2004).
4. A. R. Tumlinson, L. P. Hariri, U. Utzinger, and J. K. Barton, "Miniature endoscope for simultaneous optical coherence tomography and laser-induced fluorescence measurement," *Appl. Opt.* **43**, 113–121 (2004).
5. L. P. Hariri, A. R. Tumlinson, D. G. Besselsen, U. Utzinger, E. W. Gerner, and J. K. Barton, "Endoscopic optical coherence tomography and laser-induced fluorescence spectroscopy in a murine colon cancer model," *Lasers Surg. Med.* **38**, 305–313 (2006).
6. P. R. Herz, Y. Chen, A. D. Aguirre, J. G. Fujimoto, H. Mashimo, J. Schmitt, A. Koski, J. Goodnow, and C. Petersen, "Ultrahigh resolution optical biopsy with endoscopic optical coherence tomography," *Opt. Express* **12**, 3532–3542 (2004).
7. W. Drexler, U. Morgner, F. X. Kartner, C. Pitris, S. A. Boppart, X. D. Li, E. P. Ippen, and J. G. Fujimoto, "*In vivo* ultrahigh-resolution optical coherence tomography," *Opt. Lett.* **24**, 1221–1223 (1999).
8. X. D. Li, T. H. Ko, and J. G. Fujimoto, "Intraluminal fiber-optic Doppler imaging catheter for structural and functional coherence tomography," *Opt. Lett.* **26**, 1906–1908 (2001).
9. J. A. Izatt, M. V. Sivak, A. M. Rollins, A. Horii, T. Hirata, and S. Iizuka, "Optical imaging device," U.S. Patent No. 6,564,089 (2006).
10. A. R. Tumlinson, J. K. Barton, B. Považay, H. Sattman, A. Unterhuber, R. A. Leitgeb, and W. Drexler, "Endoscope-tip interferometer for ultrahigh resolution frequency domain optical coherence tomography in mouse colon," *Opt. Express* **14**, 1878–1887 (2006).
11. M. Gloesmann, B. Hermann, C. Schubert, H. Sattmann, P. K. Ahnelt, and W. Drexler, "Histologic correlation of pig retina radial stratification with ultrahigh-resolution optical coherence tomography," *Invest. Ophthalmol. Visual Sci.* **44**, 1696–1703 (2003).
12. B. E. Bouma and G. J. Tearney, "Power-efficient nonreciprocal interferometer and linear-scanning fiber-optic catheter for optical coherence tomography," *Opt. Lett.* **24**, 531–533 (1999).
13. Z. L. Hu and A. M. Rollins, "Quasi-telecentric optical design of a microscope-compatible OCT scanner," *Opt. Express* **13**, 6407–6415 (2005).
14. Z. Hu and A. M. Rollins, "Advanced analysis of OCT optics," in *Proc. SPIE* **5690**, 372–379 (2005).

15. E. A. Swanson, D. Huang, M. R. Hee, J. G. Fujimoto, C. P. Lin, and C. A. Puliato, "High-speed optical coherence domain reflectometry," *Opt. Lett.* **17**, 151–153 (1992).
16. U. Morgner, W. Drexler, F. X. Kartner, X. D. Li, C. Pitris, E. P. Ippen, and J. G. Fujimoto, "Spectroscopic optical coherence tomography," *Opt. Lett.* **25**, 111–113 (2000).
17. G. P. Boivin, K. Washington, K. Yang, J. M. Ward, T. P. Pretlow, R. Russell, D. G. Besselsen, V. L. Godfrey, T. Doetschman, W. F. Dove, H. C. Pitot, R. B. Halberg, S. H. Itzkowitz, J. Groden, and R. J. Coffey, "Pathology of mouse models of intestinal cancer: Consensus report and recommendations," *Gastroenterology* **124**, 762–777 (2003).
18. H. F. Yerushalmi, D. G. Besselsen, N. A. Ignatenko, K. A. Blohm-Mangone, J. L. Padilla-Torres, D. E. Stringer, H. Cui, H. Holubec, C. M. Payne, and E. W. Gerner, "The role of NO synthases in arginine-dependent small intestinal and colonic carcinogenesis," *Mol. Carcinog.* **45**, 93–105 (2006).
19. R. Suzuki, H. Kohno, S. Sugie, H. Nakagama, and T. Tanaka, "Strain differences in the susceptibility to azoxymethane and dextran sodium sulfate-induced colon carcinogenesis in mice," *Carcinogenesis* **27**, 162–169 (2006).
20. R. R. Shannon, "Aberrations," Chapter 3 in *The Art and Science of Optical Design*, pp. 164–264, Cambridge University Press, Cambridge (2006).